

Physics-constrained, low-dimensional models for MHD: First-principles and data-driven approaches

Alan A. Kaptanoglu

Department of Physics, University of Washington

Kyle D. Morgan

Department of Aeronautics and Astronautics, University of Washington

Chris J. Hansen

Department of Aeronautics and Astronautics, University of Washington

Department of Applied Physics and Applied Mathematics, Columbia University

Steven L. Brunton

Department of Mechanical Engineering, University of Washington

Abstract

Modeling and control of plasmas is a notoriously challenging, yet vital topic in modern physics. The magnetohydrodynamic (MHD) equations, for example, involve coupling between fluid dynamics and electromagnetism and exhibit nonlinear, multi-scale spatio-temporal dynamics. This work develops a novel reduced-order modeling framework for compressible plasmas, leveraging decades of progress in first-principles and data-driven modeling of fluids. First, we introduce a dimensionally consistent reduction technique to approximate the plasma in terms of a low-dimensional set of energetic coherent structures, or *modes*. Next, we derive an analytic model by Galerkin projection of the compressible Hall-MHD equations onto these modes. Importantly, we explicitly constrain the structure of the Galerkin model to enforce conservation of energy with a power balance argument. This theoretical framework enables the development of sparse and interpretable nonlinear reduced-order models from data that are intrinsically connected to the underlying physics. We demonstrate this approach on data from high-fidelity numerical simulations, tuned to model a 3D, turbulent spheromak experiment. We find excellent agreement with a low-dimensional model that describes the evolution of dominant coherent structures in the plasma. This reduced-order modeling framework demonstrates promise for the prediction, estimation, and control in industrial and laboratory plasmas.

Keywords: plasma, MHD, reduced-order modeling, Galerkin projection, machine learning

1 Introduction

Plasmas and plasma-enabled technologies are pervasive in everyday life, perhaps most notably through microchip fabrication and plasma processing of modern materials [1]. Future technologies, such as magnetic confinement fusion and electric propulsion, have tremendous potential for the continued radical reshaping of human society by the principled manipulation of plasmas. However, plasmas are notoriously challenging to model and control, as they couple both fluid dynamics and electromagnetism and are characterized by nonlinear, multi-scale behavior. Modeling plasmas often requires computationally intensive and high-dimensional simulations, precluding the use of these models for real-time control. In this work, we provide a theoretical framework for physics-constrained, low-dimensional plasma models which can be computed efficiently and show significant promise for physical discovery, prediction, and real-time control of plasmas.

Real-time control with interpretable and low-dimensional models is essential for the success of magnetic confinement fusion [2] and many other advanced plasma technologies. For example, steady-state tokamak operation will require the active control of edge-localized modes (ELMs) and divertor detachment, and the avoidance or mitigation of disruptions, which can seriously damage components of the device [3]. There are a wealth of advanced model-based control techniques [4], such as model predictive control (MPC) [5, 6], that may be leveraged for these plasma systems. However, existing models are either too high-dimensional and computationally expensive to operate in real-time or too low-fidelity to provide a useful prediction for control. Thus, there is a critical need for reduced-order models that balance fidelity and efficiency, providing a sufficiently accurate prediction fast enough to be useful for control [7].

Fortunately, many high-dimensional nonlinear systems tend to evolve on low-dimensional attractors [8, 9], defined by spatio-temporal coherent structures that characterize the dominant behavior of the system. Thus, it is possible to map the high-dimensional physical space to a lower-dimensional *feature* space, and then obtain a reduced-order model for the evolution of these coherent structures. A number of studies in the plasma physics community indicate that the vast majority of the total energy in plasma systems can be explained by fewer than ten low-dimensional coherent structures, across a large range of parameter regimes, geometry, and degree of nonlinearity [10–13]. In these cases, the evolution of only a few coherent structures can closely approximate the full evolution of the high-dimensional model.

Recent progress in theoretical, data-driven, and machine learning methods are revolutionizing the analysis, modeling, and control of high-dimensional, nonlinear systems, especially in the field of fluid mechanics [14]. Reduced-order modeling, or the process of obtaining low-dimensional models to approximate high-dimensional dynamics, is advancing particularly rapidly, enabling the modeling of increasingly complex fluid flows [4, 9, 14–20]. Many of the standard techniques for dimensionality reduction and modeling of fluids have been adopted in the plasma physics community. The biorthogonal decomposition (BOD) is a common reduced-order modeling method for plasmas [10, 12, 21–24] that is related to the proper orthogonal decomposition (POD) in fluid mechanics [8, 9]. Other techniques from fluid dynamics, such as the dynamic mode decomposition [25] which approximates the system with a linear data-driven model, are also beginning to contribute to the field of plasma physics [13, 26].

Although plasma dynamics share much in common with fluid mechanics, many advanced reduced-order modeling techniques have not yet been adopted in the plasma physics community. For example, careful development of a dimensionalized inner product have enabled the extension of POD from incompressible to compressible fluid flows [27]. It is also common in fluid mechanics to obtain nonlinear reduced-order models by Galerkin projection of the Navier-Stokes equations onto POD modes, making it possible to enforce known symmetries and conservation laws, such as conservation of energy [19, 28–31]. More recently, sparse optimization and machine learning have resulted in interpretable nonlinear models for complex fluid systems, balancing accuracy and efficiency [32–34]. A major focus of the present work is to extend these three innovations for compressible plasma dynamics, enabling a wealth of advanced modeling and control machinery.

1.1 Contributions of this work

In this work, we introduce a novel framework for the accurate and efficient reduced-order modeling of plasma physics that is both data-driven and constrained by the physics. Our data-driven approach is intrinsically tied to the underlying plasma physics, resulting in an interpretable low-dimensional nonlinear model for the dynamics that may be incorporated directly into model predictive control (MPC) [5] algorithms.

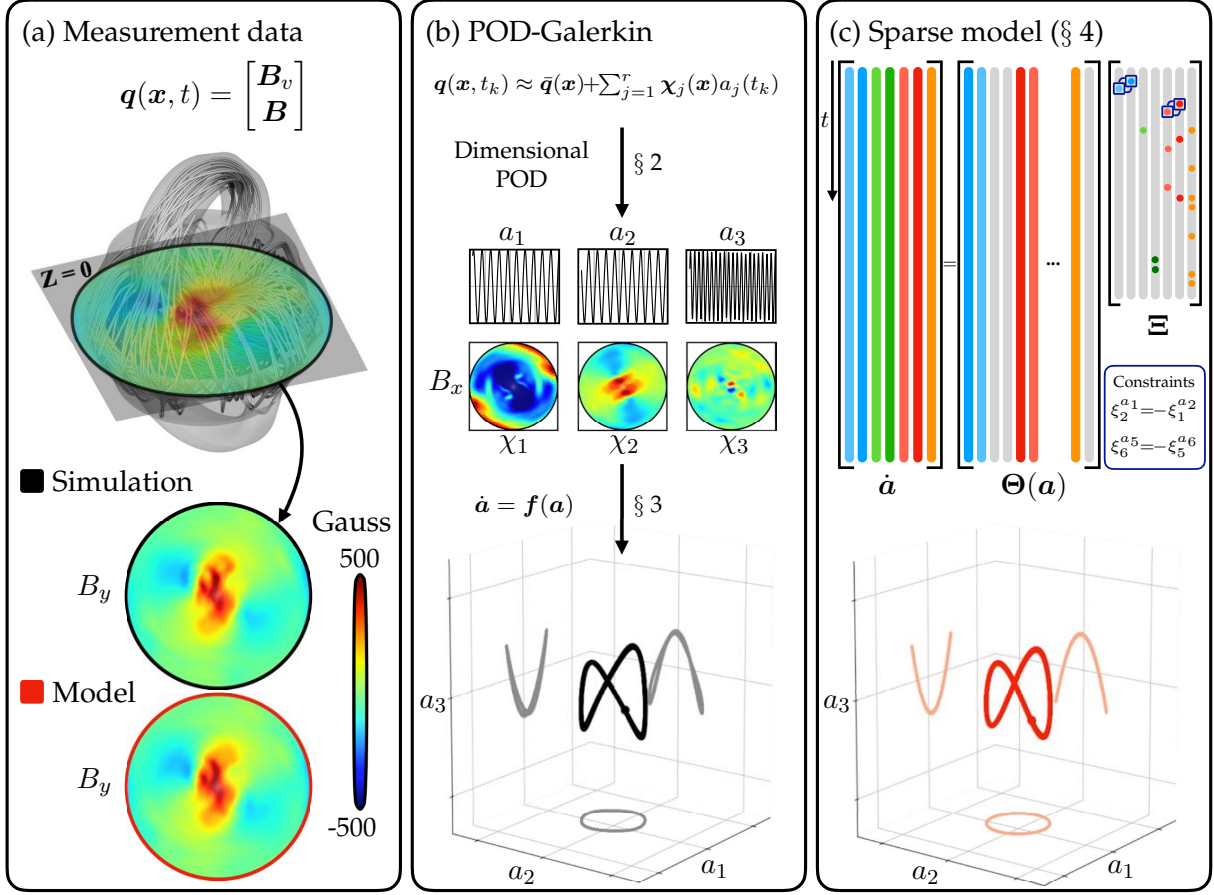


Figure 1: Overview of the data-driven plasma modeling framework proposed in this work: (a) Collect measurement data from simulations or experiments; (b) Identify spatio-temporal coherent structures and their evolution using our modified POD-Galerkin approach (see § 2, 3); and (c) develop data-driven nonlinear models using physics-constrained sparse regression (see § 4).

This work provides a *constrained POD-Galerkin model*, system of quadratic, nonlinear ordinary differential equations (ODEs) defining the time evolution of a set of low-dimensional modes. This formulation relies on the definition of a dimensionalized inner product that relates the energetic contribution of various fields and generalizes to more complicated models. Next, we derive constraints on the structure of the Galerkin model by enforcing the approximate conservation of energy in compressible Hall-MHD. The coefficients of this model may be evaluated numerically using hyper-reduction techniques [35–39]. However, we use the analytic form of the POD-Galerkin model to guide and constrain data-driven nonlinear modeling with the sparse identification of nonlinear dynamics (SINDy) method [32]. We demonstrate this unified modeling framework on high-fidelity simulations of a complicated 3D experimental plasma device. We show that a model with seven modified POD modes already captures 99% of the total energy, exhibits interesting attractor behavior, and forecasts the velocity and magnetic fields in the device with high accuracy. The proposed framework is summarized in Fig. 1. To promote reproducible research, the python code used for this analysis utilizes the PySINDy package [40] and can be found at https://github.com/akaptano/POD-Galerkin_MHD.

2 Dimensionality reduction

2.1 The proper orthogonal decomposition

The proper orthogonal decomposition (or biorthogonal decomposition, abbreviated POD or BOD) has proven useful for interpreting plasma physics data across a range of parameter regimes [10, 12, 21–24, 41, 42]. Measurements at time t_k are arranged in a vector $\mathbf{q}_k \in \mathbf{R}^D$, called a snapshot, where the dimension D is the product of the number of spatial locations and the number of variables measured at each point. The data is sampled at times t_1, t_2, \dots, t_M and arranged in a matrix

$$\mathbf{X} = \begin{array}{c} \xrightarrow{\text{time}} \\ \left[\begin{array}{cccc} q_1(t_1) & q_1(t_2) & \cdots & q_1(t_M) \\ q_2(t_1) & q_2(t_2) & \cdots & q_2(t_M) \\ \vdots & \vdots & \ddots & \vdots \\ q_D(t_1) & q_D(t_2) & \cdots & q_D(t_M) \end{array} \right] \\ \downarrow \text{state} \end{array}. \quad (1)$$

POD is based on the singular value decomposition (SVD), which provides a low-rank approximation of the data matrix $\mathbf{X} \in \mathbf{R}^{D \times M}$,

$$\mathbf{X} = \mathbf{U} \mathbf{\Sigma} \mathbf{V}^*, \quad (2)$$

where $\mathbf{U} \in \mathbf{R}^{D \times D}$ and $\mathbf{V} \in \mathbf{R}^{M \times M}$ are unitary matrices, and $\mathbf{\Sigma} \in \mathbf{R}^{D \times M}$ is a diagonal matrix containing non-negative and decreasing entries s_{jj} called the singular values of \mathbf{X} . \mathbf{V}^* denotes the complex-conjugate transpose of \mathbf{V} . The singular values indicate how important the corresponding columns of \mathbf{U} and \mathbf{V} are for describing the spatio-temporal structure of \mathbf{X} . It is often possible to discard small values of $\mathbf{\Sigma}$, resulting in a truncated matrix $\mathbf{\Sigma}_r \in \mathbf{R}^{r \times r}$. With the first $r \ll \min(D, M)$ columns of \mathbf{U} and \mathbf{V} , denoted \mathbf{U}_r and \mathbf{V}_r , the matrix \mathbf{X} can be approximated as

$$\mathbf{X} \approx \mathbf{U}_r \mathbf{\Sigma}_r \mathbf{V}_r^*. \quad (3)$$

A sensible SVD requires that the measurements in \mathbf{X} all have the same physical dimensions, and different choices of dimensionalization may lead to variations in the decomposition. The truncation rank r is typically chosen to balance accuracy and complexity [4]. Although different terminology has been used in different fields, in practice the SVD, BOD, and POD are synonymous. Sections 2.2–2.3 significantly extend this method for plasmas, and provide a theoretical structure for building constrained nonlinear models for the dynamics in this low-dimensional basis.

2.2 An inner product for plasmas

Choosing the dimensionalization of \mathbf{X} has a significant impact on the performance and energy spectrum of the resulting POD basis. Inspired by the inner product defined for compressible fluids [27], we introduce an inner product for compressible magnetohydrodynamic fluids by using the configuration vector $\mathbf{q}(\mathbf{x}, t) = [\mathbf{B}_v, \mathbf{B}, B_T]$. Here

$$\mathbf{B}_v = \sqrt{\rho \mu_0} \mathbf{v}, \quad B_T = 2\sqrt{\rho \mu_0 k_b T / m_i (\gamma - 1)}, \quad (4)$$

where \mathbf{v} is the fluid velocity, ρ is the mass density, k_b is Boltzmann's constant, μ_0 is the permeability of free space, T is the plasma temperature, m_i is the ion mass, γ is the adiabatic index, and $p = 2\rho T / m_i$ is the plasma pressure. With the exception of temperature in eV, SI units are used. \mathbf{B}_v and B_T are defined so that the following scaled inner product yields the total energy W ,

$$W = \frac{1}{2\mu_0} \langle \mathbf{q}, \mathbf{q} \rangle = \frac{1}{2\mu_0} \int (\mathbf{B}_v^2 + B^2 + B_T^2) d^3 \mathbf{x} = \int \left(\frac{1}{2} \rho v^2 + \frac{B^2}{2\mu_0} + \frac{p}{\gamma - 1} \right) d^3 \mathbf{x}. \quad (5)$$

Because of the equivalence to the total energy, this inner product is conserved for a closed system without dissipation. The total energy may also be approximately conserved without these assumptions; input power in a laboratory device may be used to balance dissipation in the volume for a steady-state or quasi steady-state plasma system [43, 44].

Despite the normalization to magnetic field units, we refrain from interpretation of this configuration vector as a generalized magnetic field because B_v is a vector, B is a pseudovector, and B_T is a scalar. To avoid a far more complicated set of differential equations, we consider the case of uniform and constant temperature, so that B_T may be omitted and q simplified to $q = [B_v, B]$. We will show in Sec. 3 that this inner product formulation allows the compressible Hall-MHD to be reformulated as a simple system of ordinary differential equations, known as a *Galerkin model*, governing the evolution of a set of temporal modes derived from q .

2.3 The dimensionalized proper orthogonal decomposition

Traditional use of the POD would either require separate decompositions for v , B , and T , or an arbitrary choice of dimensionalization. With the inner product derived above, we perform the SVD on the normalized configuration vector q . If ρ is not constant, the density must be measured, estimated, or interpolated to the location of the v measurement so that the transformation from $v \rightarrow B_v$ is possible. The matrix X^*X is then computed via the inner products

$$X^*X \approx \langle q(t_k), q(t_m) \rangle. \quad (6)$$

The method of snapshots [45] is used here because the number of snapshots is often far fewer than the number of measurements, $M \ll D$, but this is not a requirement of the dimensionalized POD method. Substitution of the SVD for the matrix X produces

$$X^*X V_r = V_r \Sigma_r^2, \quad (7)$$

an eigenvalue equation for V_r ; therefore we can obtain V_r by diagonalizing $X^*X \in \mathbf{R}^{M \times M}$ instead of computing the SVD of X . The *chronos* are the temporal SVD modes, i.e. the columns of V_r , denoted v_j . The *topos* are the spatial modes forming the columns of U_r , denoted χ . We may additionally scale these columns so that the dynamic trajectories remain on the unit ball. The normalized matrix of chronos, a , is defined so that $a_{jk} = v_{jk} / \sum_{j=1}^r \max_k |v_{jk}|$. Importantly, we have arrived at a set of spatio-temporal modes so that q may be written efficiently in the POD basis

$$q(x_i, t_k) \approx \bar{q}(x_i) + \sum_{j=1}^r \chi_j(x_i) a_j(t_k), \quad (8)$$

where we have absorbed the normalization of a_{jk} and the singular values into the definition of $\chi_j(x_i)$. By construction $\langle \chi_i, \chi_j \rangle \propto \delta_{ij}$. Here $\bar{q}(x_i)$ is assumed to be some mean or steady-state field, typically taken as the temporal average of the data. Subtracting q before performing POD guarantees that the boundary conditions are satisfied for any coefficients a [15]. In principle, we could have expanded q in any set of orthonormal modes in space and time. The advantage of the POD basis is that the modes are ordered by energy content; a truncation of the system still captures the vast majority of the dynamics. If we had separately computed POD on the velocity and magnetic fields in isolation, we would have two sets of POD modes with independent time dynamics. In contrast, the current approach captures both the velocity and magnetic fields simultaneously, resulting in a single set of temporal POD modes $a(t)$ in Eq. (8). In the next section, we will construct an efficient reduced-order model for the evolution of the mode amplitudes a

$$\dot{a} = f(a). \quad (9)$$

3 Reduced-order models for compressible Hall-MHD

Compressible Hall-MHD is useful for describing a range of space and laboratory plasmas [46]. The compressible Hall-MHD model with constant and uniform temperature is given by:

$$\dot{\rho} = -\nabla \cdot \left(\sqrt{\frac{\rho}{\mu_0}} \mathbf{B}_v \right), \quad (10)$$

$$\begin{aligned} \dot{\mathbf{B}}_v = & -\frac{1}{\sqrt{\rho\mu_0}} \left(\frac{1}{2} \mathbf{B}_v \nabla \cdot \mathbf{B}_v + \mathbf{B}_v \cdot \nabla \mathbf{B}_v - \frac{1}{4\rho} \mathbf{B}_v (\nabla \rho \cdot \mathbf{B}_v) - (\nabla \times \mathbf{B}) \times \mathbf{B} + \frac{2T\mu_0}{m_i} \nabla \rho \right) \\ & + \nu \left[\nabla^2 \mathbf{B}_v - \frac{\nabla^2 \rho}{2\rho} \mathbf{B}_v + \frac{3\mathbf{B}_v}{4\rho^2} \nabla \rho \cdot \nabla \rho + \frac{1}{\rho} (\nabla \rho \cdot \nabla) \mathbf{B}_v - \frac{1}{6\rho} \nabla (\nabla \rho \cdot \mathbf{B}_v) \right. \\ & \left. + \frac{1}{4\rho^2} (\nabla \rho \cdot \mathbf{B}_v) \nabla \rho + \frac{1}{3} \nabla (\nabla \cdot \mathbf{B}_v) - \frac{1}{6\rho} (\nabla \cdot \mathbf{B}_v) \nabla \rho \right], \end{aligned} \quad (11)$$

$$\dot{\mathbf{B}} = \nabla \times \left[\frac{1}{\sqrt{\rho\mu_0}} (\mathbf{B}_v \times \mathbf{B} - d_i (\nabla \times \mathbf{B}) \times \mathbf{B}) \right] + \frac{\eta}{\mu_0} \nabla^2 \mathbf{B}. \quad (12)$$

Note that we have dropped the electron diamagnetic term, because $\nabla \times (\nabla p / \rho)$ vanishes in the isothermal limit. Here $\nu = \tilde{\nu} / \rho$ is the dynamic viscosity, $\eta \propto T^{-\frac{3}{2}}$ is the Spitzer resistivity [47], $d_i = m_i / (e\sqrt{\rho\mu_0})$ is the ion inertial length, and $c_s = \sqrt{\gamma T / m_i}$ is the plasma sound speed. In the limit of time-independent density, we have

$$\frac{1}{2\rho} (\nabla \rho \cdot \mathbf{B}_v) = -\nabla \cdot \mathbf{B}_v, \quad (13)$$

$$\begin{aligned} \dot{\mathbf{B}}_v = & -\frac{1}{\sqrt{\rho\mu_0}} (\mathbf{B}_v (\nabla \cdot \mathbf{B}_v) + \mathbf{B}_v \cdot \nabla \mathbf{B}_v - (\nabla \times \mathbf{B}) \times \mathbf{B} + \frac{2T\mu_0}{m_i} \nabla \rho) \\ & + \nu \left[\nabla^2 \mathbf{B}_v - \frac{\nabla^2 \rho}{2\rho} \mathbf{B}_v + \frac{3\mathbf{B}_v}{4\rho^2} \nabla \rho \cdot \nabla \rho + \frac{1}{\rho} (\nabla \rho \cdot \nabla) \mathbf{B}_v + \frac{2}{3} \nabla (\nabla \cdot \mathbf{B}_v) - \frac{1}{3\rho} (\nabla \cdot \mathbf{B}_v) \nabla \rho \right], \end{aligned} \quad (14)$$

$$\dot{\mathbf{B}} = \nabla \times \left[\frac{1}{\sqrt{\rho\mu_0}} (\mathbf{B}_v \times \mathbf{B} - d_i (\nabla \times \mathbf{B}) \times \mathbf{B}) \right] + \frac{\eta}{\mu_0} \nabla^2 \mathbf{B}. \quad (15)$$

In this limiting case, the compressible MHD model is exactly quadratic in the temporal dependence and can be recast in a form separating out the constant, linear, and quadratic parts:

$$\begin{aligned} \dot{\mathbf{q}} &= \mathbf{C} + \mathbf{L}(\mathbf{q}) + \mathbf{Q}(\mathbf{q}, \mathbf{q}), \quad (16) \\ \mathbf{C} &= \begin{bmatrix} -\frac{2T}{m_i} \sqrt{\frac{\mu_0}{\rho}} \nabla \rho \\ 0 \end{bmatrix}, \\ \mathbf{L}(\mathbf{q}) &= \begin{bmatrix} \nu \left(\nabla^2 \mathbf{B}_v - \frac{1}{2\rho} \mathbf{B}_v \nabla^2 \rho + \frac{3}{4\rho^2} (\nabla \rho \cdot \nabla \rho) \mathbf{B}_v + \frac{1}{\rho} (\nabla \rho \cdot \nabla) \mathbf{B}_v + \frac{2}{3} \nabla (\nabla \cdot \mathbf{B}_v) - \frac{1}{3\rho} (\nabla \cdot \mathbf{B}_v) \nabla \rho \right) \\ \frac{\eta}{\mu_0} \nabla^2 \mathbf{B} \end{bmatrix}, \\ \mathbf{Q}(\mathbf{q}, \mathbf{q}) &= \begin{bmatrix} -\frac{1}{\sqrt{\rho\mu_0}} (\mathbf{B}_v (\nabla \cdot \mathbf{B}_v) + \mathbf{B}_v \cdot \nabla \mathbf{B}_v - (\nabla \times \mathbf{B}) \times \mathbf{B}) \\ \nabla \times \left(\frac{1}{\sqrt{\rho\mu_0}} (\mathbf{B}_v \times \mathbf{B} - d_i (\nabla \times \mathbf{B}) \times \mathbf{B}) \right) \end{bmatrix}. \end{aligned}$$

This is intentionally written in a form that has the same structure as in fluid mechanics [27], allowing us to derive the Galerkin model in Sec. 3.1. The nonlinearities are considerably more complicated (i.e. not quadratic) with the full temporal evolution of the density and temperature. However, data-driven models from simulations using full spatio-temporal density evolution in Sec. 5.2 are quite accurate. Moreover, increasingly sophisticated models may be tractable in future work, since the data-driven SINDy approach is not limited to quadratic nonlinearities.

3.1 Galerkin model for compressible Hall MHD

Substituting the dimensionalized POD basis expansion of \mathbf{q} into Eq. (16) results in a set of quadratic ordinary differential equations for compressible Hall-MHD. These efficient Galerkin models are common in the fluid mechanics communities. Expanding \mathbf{q} in the dimensionalized POD basis from Eq. (8) and utilizing the orthonormality of the χ_j produces the following Galerkin model:

$$\begin{aligned} \dot{a}_j(t) &= C^0 + C_j^1 + C_j^2 + \sum_{i=1}^r (L_{ij}^1 + L_{ij}^2) a_i + \sum_{h,i=1}^r Q_{hij} a_h a_i, \\ C^0 &= \langle \mathbf{C}, \chi_j \rangle, \\ C_j^1 &= \langle \mathbf{L}(\bar{\mathbf{q}}), \chi_j \rangle, \\ C_j^2 &= \langle \mathbf{Q}(\bar{\mathbf{q}}, \bar{\mathbf{q}}), \chi_j \rangle, \\ L_{ij}^1 &= \langle \mathbf{L}(\chi_i), \chi_j \rangle, \\ L_{ij}^2 &= \langle \mathbf{Q}(\bar{\mathbf{q}}, \chi_i) + \mathbf{Q}(\chi_i, \bar{\mathbf{q}}), \chi_j \rangle, \\ Q_{hij} &= \langle \mathbf{Q}(\chi_h, \chi_i), \chi_j \rangle. \end{aligned} \quad (17)$$

The inner products integrate out the spatial dependence, and the model is quadratic in the temporal POD modes $a_j(t)$. If $\bar{\mathbf{q}}$ satisfies the steady-state MHD equations, then $C^0 + C_j^1 + C_j^2 = 0$. This is a reasonable assumption for any approximately steady-state device, such as a tokamak, which can be sustained on the order of seconds. In contrast to Eq. (17), a Galerkin model based on separate POD expansions for each field would involve significantly more complicated nonlinear terms from mixing and a lack of orthonormality $\langle \chi_i^v, \chi_j^B \rangle \neq \delta_{ij}$ between the POD modes for \mathbf{v} and \mathbf{B} .

Although Eq. (17) contains only quadratic nonlinearities, a cubic or higher-order model may approximate the dynamics associated with truncated POD modes [33]. In the fluids community, it has been shown for the von Karman vortex street that the influence of low-energy modes can be accounted for by including cubic nonlinearities in the truncated Galerkin model [33, 48], which is related to center-manifold reduction [49].

The inner products in this Galerkin model can be computed from measurements of the fields and their first and second derivatives. Therefore, for an explicit calculation of these coefficients, the first and second order spatial derivatives for ρ , \mathbf{B}_v , and \mathbf{B} must be well-approximated in the region of experimental interest. In some cases, high-resolution diagnostics on experimental devices can resolve these quantities in a particular region of the plasma. However, even if this data is available, computing these inner products and evaluating the nonlinear terms in the model is expensive, because the fields have the original spatial dimension D . Fortunately, there are hyper-reduction techniques from fluid dynamics, such as the discrete empirical interpolation method (DEIM) [37], QDEIM [39], and gappy POD [35, 36, 38], which enable efficient computations.

3.2 Conservation of energy

It is possible to constrain the Galerkin model above to conserve energy, through a power balance of input power and dissipation in the plasma. Compressible Hall-MHD in the limit of constant and uniform temperature produces (see Galtier [50] Eq. 3.22)

$$\begin{aligned} \frac{\partial W}{\partial t} &= - \oint \left[\left(\frac{1}{2} \rho v^2 + p \right) \mathbf{v} + \mathbf{P} - \frac{4}{3} \tilde{\nu} (\nabla \cdot \mathbf{v}) \mathbf{v} - \tilde{\nu} \mathbf{v} \times (\nabla \times \mathbf{v}) \right] \cdot \hat{\mathbf{n}} dS \\ &\quad - \int \left[\tilde{\nu} (\nabla \times \mathbf{v})^2 + \eta (\nabla \times \mathbf{B})^2 + \frac{4}{3} \tilde{\nu} (\nabla \cdot \mathbf{v})^2 \right] d^3 \mathbf{x}. \end{aligned} \quad (18)$$

Here \hat{n} is a unit normal vector to the boundary, $\mathbf{P} = \mu_0^{-1} \mathbf{E} \times \mathbf{B}$ is the Poynting vector (\mathbf{E} is the electric field), which is in principle an imposed and experimentally-known function of space and time. To simplify, we assume that the boundary conditions satisfy $\mathbf{v} \cdot \hat{n} = \mathbf{v} \times \hat{n} = 0$ and $\mathbf{B} \cdot \hat{n} = 0$ at the wall, zeroing all the surface terms except for the Poynting flux. These condition are satisfied for the simulation presented in Sec. 5.2. Then we have

$$\begin{aligned} \frac{\partial W}{\partial t} &= - \oint \mathbf{P} \cdot \hat{n} dS - \int \left[\tilde{\nu} (\nabla \times \mathbf{v})^2 + \eta (\nabla \times \mathbf{B})^2 + \frac{4}{3} \tilde{\nu} (\nabla \cdot \mathbf{v})^2 \right] d^3 \mathbf{x} \\ &= - \oint \mathbf{P} \cdot \hat{n} dS - \int \left[\nu (\nabla \times \mathbf{B}_v - \frac{\nabla \rho}{2\rho} \times \mathbf{B}_v)^2 + \eta (\nabla \times \mathbf{B})^2 + \frac{4}{3} \nu (\nabla \cdot \mathbf{B}_v - \frac{\nabla \rho}{2\rho} \cdot \mathbf{B}_v)^2 \right] d^3 \mathbf{x}. \end{aligned} \quad (19)$$

In steady-state, W is approximately conserved as the injected power balances the dissipative losses. In any orthonormal basis, the injected power must separately balance the terms which are linear and quadratic in the temporal modes. To reflect this, the power is split into

$$\oint \mathbf{P} \cdot \hat{n} dS = \sum_{i=1}^r P_i^{\text{linear}} a_i + \sum_{i,j=1}^r P_{ij}^{\text{quadratic}} a_i a_j. \quad (20)$$

Then we can expand the fields in the POD modes to obtain:

$$\begin{aligned} 0 &\approx \frac{\partial W}{\partial t} \implies 0 \approx \sum_i W_i^{\text{linear}} a_i, \quad 0 \approx \sum_{i,j=1} W_{ij}^{\text{quadratic}} a_i a_j, \\ W_i^{\text{linear}} &= P_i^{\text{linear}} + 2 \int \left[\nu (\nabla \times \bar{\mathbf{B}}_v - \frac{\nabla \rho}{2\rho} \times \bar{\mathbf{B}}_v) \cdot (\nabla \times \chi_i^{B_v} - \frac{\nabla \rho}{2\rho} \times \chi_i^{B_v}) + \eta (\nabla \times \bar{\mathbf{B}}) \cdot (\nabla \times \chi_i^B) \right. \\ &\quad \left. + \frac{4}{3} \nu (\nabla \cdot \bar{\mathbf{B}}_v - \frac{\nabla \rho}{2\rho} \cdot \bar{\mathbf{B}}_v) \cdot (\nabla \cdot \chi_i^{B_v} - \frac{\nabla \rho}{2\rho} \cdot \chi_i^{B_v}) \right] d^3 \mathbf{x}, \\ W_{ij}^{\text{quadratic}} &= P_{ij}^{\text{quadratic}} + \int \left[\nu (\nabla \times \chi_i^{B_v} - \frac{\nabla \rho}{2\rho} \times \chi_i^{B_v}) \cdot (\nabla \times \chi_j^{B_v} - \frac{\nabla \rho}{2\rho} \times \chi_j^{B_v}) + \eta (\nabla \times \chi_i^B) \cdot (\nabla \times \chi_j^B) \right. \\ &\quad \left. + \frac{4}{3} \nu (\nabla \cdot \chi_i^{B_v} - \frac{\nabla \rho}{2\rho} \cdot \chi_i^{B_v}) \cdot (\nabla \cdot \chi_j^{B_v} - \frac{\nabla \rho}{2\rho} \cdot \chi_j^{B_v}) \right] d^3 \mathbf{x}. \end{aligned} \quad (21)$$

We used the fact that the mean field, by solving the steady-state Hall-MHD equations, satisfies

$$\begin{aligned} \frac{\partial W_{\min}}{\partial t} = 0 &= - \int \left[\nu (\nabla \times \bar{\mathbf{B}}_v - \frac{\nabla \rho}{2\rho} \times \bar{\mathbf{B}}_v) \cdot (\nabla \times \bar{\mathbf{B}}_v - \frac{\nabla \rho}{2\rho} \times \bar{\mathbf{B}}_v) \right. \\ &\quad \left. + \eta (\nabla \times \bar{\mathbf{B}}) \cdot (\nabla \times \bar{\mathbf{B}}) + \frac{4}{3} \nu (\nabla \cdot \bar{\mathbf{B}}_v - \frac{\nabla \rho}{2\rho} \cdot \bar{\mathbf{B}}_v) \cdot (\nabla \cdot \bar{\mathbf{B}}_v - \frac{\nabla \rho}{2\rho} \cdot \bar{\mathbf{B}}_v) \right] d^3 \mathbf{x}. \end{aligned} \quad (22)$$

The evolution equation for \mathbf{q} satisfies

$$\int \frac{1}{2} \frac{\partial q^2}{\partial t} d^3 \mathbf{x} = \sum_{i,j=1}^r a_i \frac{\partial a_j}{\partial t} \int \chi_i \chi_j d^3 \mathbf{x} = a_i \dot{a}_i = \frac{\partial W}{\partial t} - \int \rho c_s^2 (\nabla \cdot \mathbf{v}) d^3 \mathbf{x}. \quad (23)$$

The extra term arises since B_T was omitted in the \mathbf{q} vector. This term is small for low-temperature or mildly compressible plasmas, so we neglect it. Including B_T would remove this term but produce a model with higher order nonlinearities. The Galerkin model in vector notation is

$$\mathbf{a}^T \cdot \dot{\mathbf{a}} = \mathbf{a}^T (\mathbf{L}^1 + \mathbf{L}^2) \mathbf{a} + \mathbf{a}^T \mathbf{Q} \mathbf{a} \mathbf{a}. \quad (24)$$

All of the quadratic nonlinearities are in $\mathbf{a}^T (\mathbf{L}^1 + \mathbf{L}^2) \mathbf{a}$. Since we have assumed that $\bar{\mathbf{q}}$ is steady-state, there are no linear terms in Eq. (24), so $\mathbf{W}^{\text{linear}}$ is identically zero. However, conservation of energy does constrain the linear structure of the model so that \mathbf{L}^1 and \mathbf{L}^2 satisfy $\mathbf{a}^T (\mathbf{L}^1 + \mathbf{L}^2) \mathbf{a} \approx 0$. We can incorporate this constraint directly into our data-driven model discovery procedure.

4 Nonlinear model discovery

Rather than explicitly computing the coefficients of the Galerkin model, requiring resolution of the fields and their spatial derivatives beyond what is typically experimentally feasible, it is instead possible to leverage emerging techniques in machine learning and optimization to discover these models from data [4]. Several recent approaches have enabled the data-driven identification of nonlinear dynamical systems models that balance model complexity and descriptive capability [32, 51]. Here, we will use the sparse identification of nonlinear dynamics (SINDy) algorithm [32] to identify nonlinear reduced-order models for plasmas. SINDy models are *parsimonious*, having as few terms as are required to explain the dynamics, which in turn promotes models that are interpretable, prevent overfitting, and tend to generalize to new situations that were not in the training data. Importantly, the SINDy framework enables the discovery of models that enforce physics-based constraints, such as energy conservation, by construction [33].

The SINDy algorithm is based on the observation that dynamical systems, given by systems of ordinary differential equations, often have only a few active terms that define the dynamics, so that the dynamics may be represented *sparingly* in a library of candidate terms. Our goal is to identify a low-dimensional model for the time-evolution of $\mathbf{a}(t)$, the vector of POD mode amplitudes, as a sparse linear combination of elements from a library of candidate terms $\Theta = [\theta_1(\mathbf{a}) \ \theta_2(\mathbf{a}) \ \cdots \ \theta_p(\mathbf{a})]$:

$$\frac{d}{dt}\mathbf{a} = \mathbf{f}(\mathbf{a}) \approx \Theta(\mathbf{a})\Xi. \quad (25)$$

The matrix $\Xi = [\xi_1 \ \xi_2 \ \cdots \ \xi_r]$ is sparse, and the nonzero elements in each column ξ_k indicate which terms are active in the dynamics of $\dot{\mathbf{a}}_k(t)$. In the case of a plasma or a fluid flow, where the physical laws are known, it is possible to construct the library Θ to include terms in the governing equations. For example, we may construct Θ with linear and quadratic terms; higher-order terms may also be included to model the effect of truncated POD modes [33].

It is possible to identify the coefficients of the sparse matrix Ξ , and thus the reduced-order model in Eq. (25), via sparse regression, leveraging measurement data from the system of interest. First, we collect a data matrix \mathbf{A} that is constructed from trajectory data:

$$\mathbf{A} = \begin{bmatrix} \mathbf{a}^T(t_1) \\ \mathbf{a}^T(t_2) \\ \vdots \\ \mathbf{a}^T(t_M) \end{bmatrix}. \quad (26)$$

Note that this data matrix $\mathbf{A} \in \mathbb{R}^{M \times r}$ transposes the data matrix convention introduced in Eq. (1). It is possible to construct a similar matrix $\dot{\mathbf{A}}$ of time derivatives, either by measuring the derivatives $\dot{\mathbf{a}}(t)$ or approximating them numerically from $\mathbf{a}(t)$. It is also possible to evaluate the library Θ on the data matrix \mathbf{A} . In the case of polynomial candidate functions, this library becomes

$$\Theta(\mathbf{A}) = \left[\begin{array}{c|c|c|c} \mathbf{A} & \mathbf{A}^{P_2} & \mathbf{A}^{P_3} & \cdots \end{array} \right]. \quad (27)$$

Higher polynomials are denoted as \mathbf{A}^{P_2} , \mathbf{A}^{P_3} , etc. Quadratic nonlinearities in \mathbf{A} are given by \mathbf{A}^{P_2} ,

$$\mathbf{A}^{P_2} = \begin{bmatrix} a_1^2(t_1) & a_1(t_1)a_2(t_1) & \cdots & a_r^2(t_1) \\ a_1^2(t_2) & a_1(t_2)a_2(t_2) & \cdots & a_r^2(t_2) \\ \vdots & \vdots & \ddots & \vdots \\ a_1^2(t_M) & a_1(t_M)a_2(t_M) & \cdots & a_r^2(t_M) \end{bmatrix}.$$

Finally, it is possible to express Eq. (25) in terms of these data matrices

$$\frac{d}{dt}\mathbf{A} = \mathbf{\Theta}(\mathbf{A})\mathbf{\Xi}. \quad (28)$$

The sparse matrix of coefficients $\mathbf{\Xi}$ may be identified via sparse regression, for example by sequentially thresholded least-squares [32, 40], LASSO [52], sparse regularized relaxed regression (SR3) [53], among other algorithms. Although less sparse models may better fit the training data, they are liable to overfit to experimental noise, resulting in overly complex models that may not generalize and have disadvantageous stability properties.

Motivated by the Galerkin model in Sec. 3, we restrict the library of candidate terms to first and second order polynomials in $\mathbf{a}(t)$, although this is not a requirement of the SINDy algorithm. The sparse vectors of coefficients $\mathbf{\Xi} = [\xi_1 \ \xi_2 \ \cdots \ \xi_r]$ may also be written in vectorized form as

$$\xi = [\xi_1^{a_1}, \dots, \xi_p^{a_1}, \xi_1^{a_2}, \dots, \xi_p^{a_2}, \dots, \xi_1^{a_r}, \dots, \xi_p^{a_r}]. \quad (29)$$

A given element $\xi_j^{a_k}$ is the coefficient on the j -th library function θ_j in the a_k row equation in Eq. (25); there are p library functions and r POD mode amplitudes.

To incorporate physics-based constraints into our data-driven model, we consider the energy conservation in the compressible Hall-MHD model derived in Sec. 3. The vanishing of the quadratic term in $\mathbf{a}^T \dot{\mathbf{a}}$ leads to an anti-symmetry constraint on the linear coefficient matrix

$$\begin{bmatrix} \xi_1^{a_1} & \xi_2^{a_1} & \xi_3^{a_1} & \cdots & \xi_r^{a_1} \\ \xi_1^{a_2} & \xi_2^{a_2} & \xi_3^{a_2} & \cdots & \xi_r^{a_2} \\ \xi_1^{a_3} & \xi_2^{a_3} & \xi_3^{a_3} & \cdots & \xi_r^{a_3} \\ \vdots & \vdots & \vdots & \ddots & \vdots \\ \xi_1^{a_r} & \xi_2^{a_r} & \xi_3^{a_r} & \cdots & \xi_r^{a_r} \end{bmatrix} = \begin{bmatrix} 0 & \xi_2^{a_1} & \xi_3^{a_1} & \cdots & \xi_r^{a_1} \\ -\xi_2^{a_1} & 0 & \xi_3^{a_2} & \cdots & \xi_r^{a_2} \\ -\xi_3^{a_1} & -\xi_3^{a_2} & 0 & \cdots & \xi_r^{a_3} \\ \vdots & \vdots & \vdots & \ddots & \vdots \\ -\xi_r^{a_1} & -\xi_r^{a_2} & -\xi_r^{a_3} & \cdots & 0 \end{bmatrix}. \quad (30)$$

For general polynomial models without a constant term, the origin is a fixed point, and the linear coefficient matrix represents the linearized system about the origin. A real, anti-symmetric matrix has eigenvalues that are either zero or come in purely imaginary pairs, so that stability must be determined through center manifold reduction or via a Lyapunov function.

The anti-symmetry constraint on the linear coefficients in Eq. (30) may be formulated as a linear equality constraint, $\mathbf{C}\xi = \mathbf{d}$, where \mathbf{C} is a constraint matrix, and \mathbf{d} is a vector of desired values; note that \mathbf{C} here is not to be confused with the coefficient matrix in the Galerkin model in Sec. 3. This constrained SINDy formulation was first introduced to conserve energy in incompressible fluid systems [33]. They showed that the sequentially thresholded least squares algorithm in the original SINDy algorithm [32] is readily adapted to include linear equality constraints. It is also possible to incorporate more general constraints using SR3 [54].

Data-driven reduced-order models for more sophisticated plasma dynamics may be tractable in the SINDy framework, since it is possible to expand the library $\mathbf{\Theta}$ to include more complex candidate dynamics. Future adoption of these methods in the plasma physics community is crucial to the development of principled data-driven control for laboratory devices.

5 Numerical results

The theoretical structure of our reduced-order modeling framework is appealing, but its practical value to the community ultimately depends on the quality of the analysis when applied to complex plasmas. In Sections 5.1 and 5.2, guided by the theoretical analysis and energy constraint derived above, a data-driven SINDy model is constructed from simulations of a 3D turbulent experimental device.

5.1 Simulations of the HIT-SI experiment

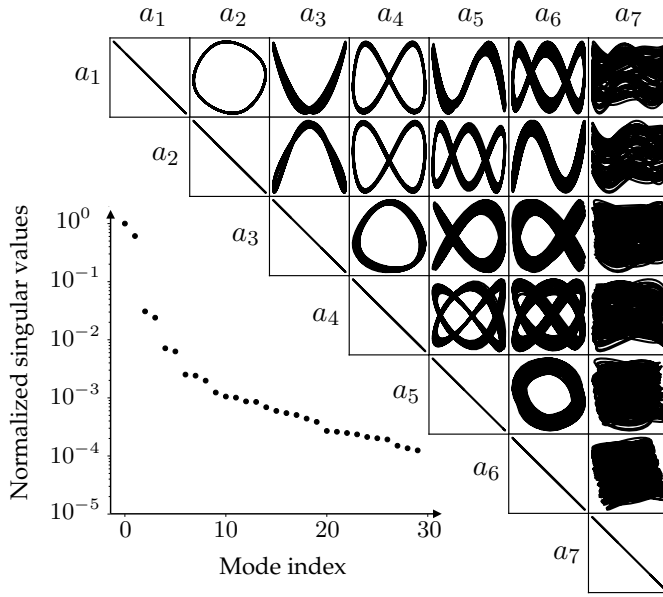
HIT-SI was a laboratory device that formed and sustained spheromak plasmas for the study of plasma self-organization and steady inductive helicity injection (SIHI) [43]. It consisted of an axisymmetric flux conserver and two inductive injectors mounted on each end, which were typically operated to produce toroidal $n = 1$ magnetic perturbations at a frequency $f_{\text{inj}} = 14.5$ kHz. Detailed descriptions of the experiment can be found in Jarboe et. al. [43] and Wrobel [55]. Compressible Hall-MHD simulations of the HIT-SI experiment in NIMROD [56] provide a robust test for the proposed framework because they are well-studied [57–61], and they involve turbulent and driven 3D plasma systems with large magnetic perturbations, $|\delta \mathbf{B}|/|\mathbf{B}| \approx 10\%$, and density perturbations, $\delta \rho/\rho \approx 100\%$, in contrast to many other fusion devices, such as tokamaks, with $|\delta \mathbf{B}|/|\mathbf{B}| \leq 0.1\%$ [44]. We restrict our study to constant and uniform temperature to match the theoretical framework presented earlier, but allow for full density evolution.

For the simulations presented in Sections 5.2–5.3, the density, velocity, and magnetic field are sampled at a set of equally-spaced points in the volume, with $\Delta\phi = \pi/16$, $\Delta R \approx \Delta Z \approx 2$ cm. The temporal resolution of the measurements varies but is typically $\Delta t_k \approx 1$ μs . The analysis presented in Sec. 5.2 is essentially unchanged for time steps as large as 10 μs , but smaller time steps are required in HIT-SI to resolve harmonics of f_{inj} that appear in the temporal POD modes. For instance, at $\Delta t_k = 10$ μs , the fourth injector harmonic is sampled on average less than twice per period. The spatial POD modes, illustrated on the $Z = 0$ midplane in the following figures, are constructed from 1440 measurement locations; the location of this midplane in the spheromak is shown in Fig. 1(a). With a non-uniform set of 50 points in the midplane, the spatial dependence changes very little, beyond smoothing out the shortest wavelengths. The fact that the HIT-SI plasma is *driven* may improve the performance of a reduced-order model, as the velocity and magnetic field exhibit similar frequency locking with the injector frequency f_{inj} and its harmonics. However, as is shown in Sec. 5.3, this can also lead to a more complicated modeling process for some modes because the frequency content of the driven modes are dominated by the injector frequency and its harmonics.

5.2 POD modes in compressible Hall-MHD simulations of HIT-SI

An examination of the structure and energy content of the POD modes can lead to physical discovery and informs an appropriate choice for the model truncation. The normalized singular values and first seven normalized POD modes are illustrated in Fig. 2. The singular values indicate that a modest model truncated at $r = 7$ already captures 99% of the total energy content; recall that the mean field has been subtracted. The first six temporal modes are approximately monochromatic, mostly representing waveforms oscillating at the injector frequency or its harmonics. However, there is significant low frequency content in the seventh mode, which appears uncorrelated with the injector frequency. Each pair of temporal modes is also illustrated in the 2D feature space in Fig. 2(a). Mode pairs 1-2, 3-4, and 5-6 all approximately behave as harmonic oscillators, although there are some significant deviations for modes 5-6. Most of the pairs exhibit a clear low-dimensional attractor where the dynamics evolve. The spatial modes in Fig. 2 exhibit considerably more structure than the temporal modes, because the Hall term leads to dispersive whistler waves, which produce short wavelength features. Although a number of short wavelength features are captured by the spatial modes, the extent to which the whistler wave dynamics are captured in the low-dimensional representation is unclear. Future work using multi-resolution techniques [62, 63] may facilitate disambiguation of the dynamics at large and small spatial scales. The fact that these spatial modes all clearly exhibit significant structure, such as visible long-range

(a) Pairwise correlations of POD amplitudes



(b) Spatial POD modes

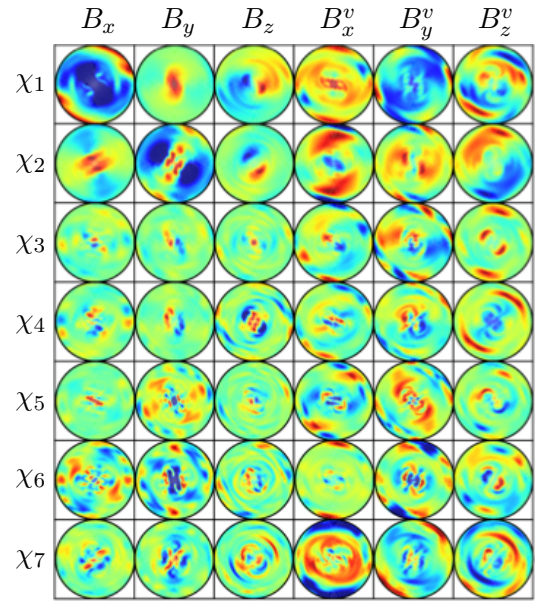
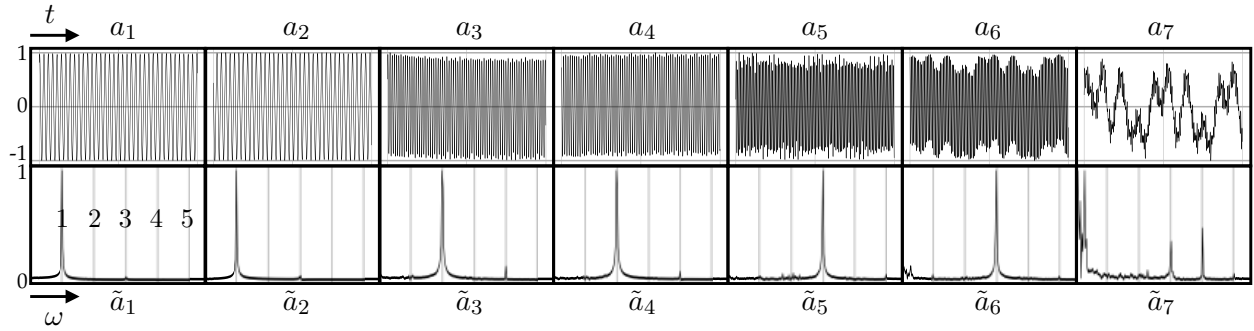
(c) Time evolutions $a(t)$ and Fourier transforms $\tilde{a}(\omega)$ 

Figure 2: Illustration of the first seven POD modes: (a) Feature space trajectories of every mode pair and the normalized singular values; (b) Spatial modes in the $Z = 0$ midplane normalized to ± 1 for visualization; (c) Time and frequency dependence indicate harmonics and peak-splitting at f_{inj} . The gray lines in the Fourier space indicate the first five harmonics of f_{inj} .

correlations and symmetry, further motivates a low-dimensional model for the evolution of these coherent modes.

5.3 Forecasting performance

The ultimate test of a data-driven model is its forecasting performance on a new dataset that was not used for training. We construct a nonlinear model using data from 1.5-3.5 ms of a NIMROD simulation, and test it on the next 0.5 ms. An analysis of the identified model can be found in Appendix A. The identified model evolution of $(a_1, a_2, a_3, a_4, a_5, a_6, a_7)$ indicates excellent agreement with the ground truth data, as shown in Fig. 3. This illustration examines the temporal evolution of the POD mode amplitudes, a sample probe measurement reconstruction, and the $Z = 0$ midplane reconstructions; for all cases except the low frequency components of mode seven, the agreement is excellent. Linked movies in Fig. 3 of $(B_x, B_y, B_z, B_x^v, B_y^v, B_z^v)$ indicate that the model accurately forecasts the entire spatio-temporal structure for all the measured quantities, although the time evolution of B_v appears to be more complex than that of B ; this extra structure is not captured by such a simple model. The reduced-order model performance is excellent, especially

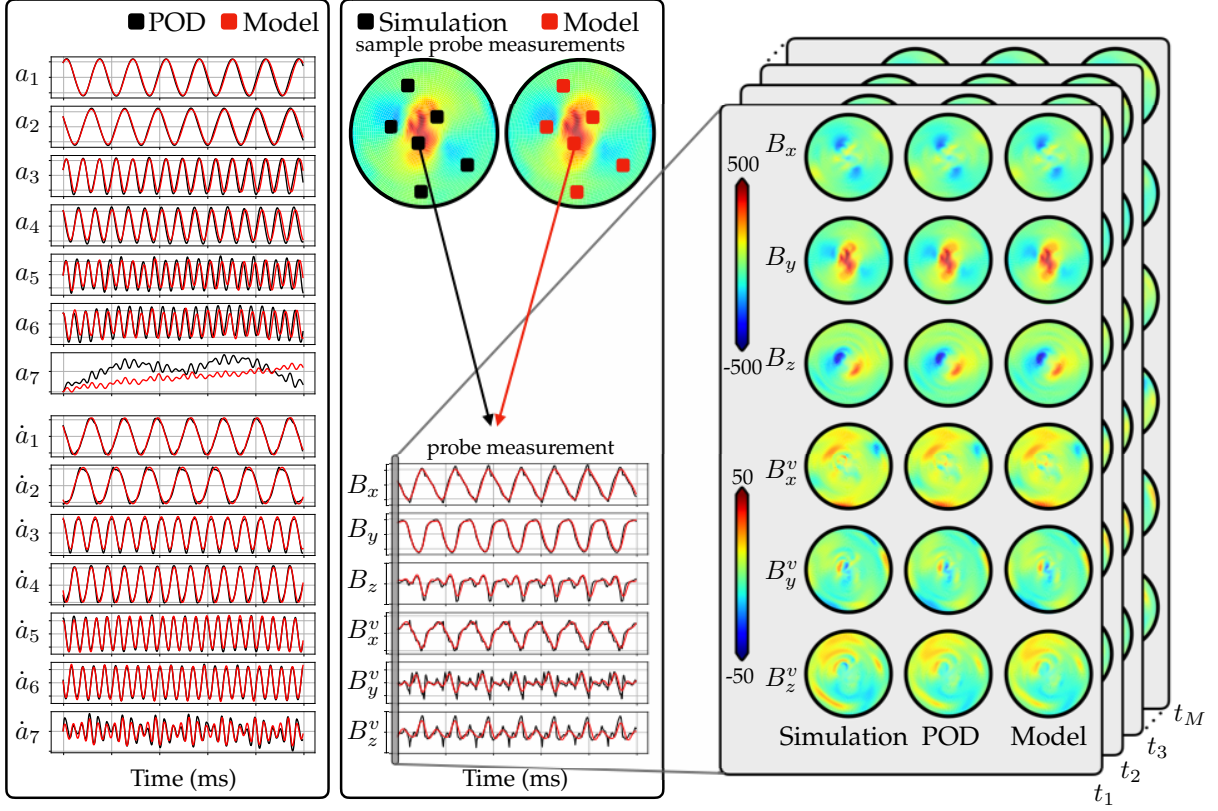


Figure 3: Model evaluation on a validation data set indicates high accuracy forecasting of the full simulation and its POD approximation. The fields $(B_x, B_y, B_z, B_x^v, B_y^v, B_z^v)$ are reported in Gauss and illustrated in the $Z = 0$ midplane for the first snapshot in the validation data.

for a $r = 7$ system of quadratic ODEs with only 18 active terms out of 245 possible terms; seven of these terms are used to model \dot{a}_7 . This seven-dimensional model forecasts much of the time evolution for a high-dimensional simulation which typically uses $96 \times 96 \times 64 = 589,824$ grid points. This SINDy model is smaller in dimension by a factor of approximately 84,000.

6 Summary and future work

We have developed a novel reduced-order modeling framework to the plasma physics community that is both data-driven and physics-constrained. By introducing a dimensionalized POD expansion for plasmas, we are able to derive a Galerkin model for the evolution of these dominant modes in time. Furthermore, we derive model constraints that enforce energy conservation in the model. This framework enables the data-driven identification of sparse, nonlinear reduced-order models that are both highly efficient and accurate. We demonstrate this approach for compressible Hall-MHD plasmas in the limit of constant and uniform temperature, with data from high-fidelity numerical simulations of a turbulent 3D experimental configuration. This framework may be used more broadly for discovering low-dimensional models, forecasting measurements, or real-time control of complex plasmas.

Alternative approaches in the tokamak literature have approached disruption avoidance and mitigation using neural networks, random forests, and other black or gray-box machine learning algorithms [54, 64–71]. Most of these models operate by training on a large number of similar

discharges to discover disruption precursors; these precursors can be used as warning signs to trigger disruption mitigation. These are useful techniques, but many of them are disconnected from the underlying plasma physics, limiting their extension to new devices and different parameter regimes. These algorithms also tend to use equilibrium plasma parameters, such as q_{95} (the safety factor at 95% of the plasma minor radius) and the elongation, which must be reconstructed from the raw data with codes such as EFIT [72]. This additional reconstruction introduces computational latency, which is known to degrade control performance. In contrast, our proposed framework utilizes the raw data directly, does not in principle require multiple discharges, directly connects to the underlying plasma physics, builds an interpretable low-dimensional nonlinear model for the dynamics, and may be incorporated directly into a real-time control algorithm such as MPC. However, this framework remains to be proven on experimental data.

Extending the proposed method to experimental data will likely introduce additional complications of noise, measurement sparsity, and completeness. By construction, the SINDy algorithm promotes sparsity in order to avoid overfitting for noisy experimental data. Although the present work relied on a data matrix constructed from a number of well-sampled, equally-spaced point measurements of the density, velocity, and magnetic field, this framework generalizes naturally to sparse experimental or simulation data with non-uniform grid spacing on arbitrary geometries. Explicit calculation of POD-Galerkin models with DEIM and QDEIM can help inform requirements on sensor placement to resolve the dynamics of interest. In order to avoid the requirement of point velocity measurements, uncommon in laboratory plasma diagnostics, a similar framework may be possible for a particular set of chord-averaged measurements. A dual approach, using time-resolved sensor data and chord-averaged measurements, similar to the approach in fluid dynamics with particle image velocimetry [34], may improve the applicability of this work to experimental data.

Future theoretical work includes the investigation of more sophisticated POD-Galerkin models for the large number of MHD variations used in the plasma physics community. A possible route for real-time control is to incorporate these models into the model predictive control framework [6]. Incorporating this framework into current devices, with reliable and diverse plasma measurements available in some region, could yield significant improvements over traditional real-time application of the POD, which tends to rely on building machine-specific markers of linear MHD instability [22, 41, 73]. In contrast, our framework could attempt to detect possible instability through deviation of the nonlinear evolution in the POD feature space from a well-traversed attractor, and could attempt actuation to push the dynamics back onto the attractor. Discovery of these low-dimensional nonlinear attractors in tokamaks could bolster the identification and control of zonal flows [11] and divertor detachment, as well as the avoidance and mitigation of disruptions [74, 75] critical to the performance of the ITER device [2]. This approach would be highly generalizable and not limited to detection of linear MHD instabilities.

There are three primary open questions that arise, regarding the procedure detailed in the present work: 1) can we remove the restriction to linear subspaces of the original state space?; 2) can we remove the requirement that the spatial POD modes are global in space (although this method may be applied to a specific region in the plasma)?; and, 3) can we ameliorate some of the difficulty in finding stable SINDy models as the system of ODEs grows in size? Fortunately, the first two considerations have been the focus of significant attention in the fluid dynamics and applied mathematics communities. Manifold Galerkin projection, relying on deep convolutional autoencoders [76], produces reduced-order models on nonlinear manifolds, although application of this method likely requires offline training. For models that are local rather than global in space, there are multi-resolution techniques based on wavelets [77], such as multi-resolution dynamic mode decomposition [62] or multi-resolution POD [63]. These spatially-localized reduced-order

models are ideal because wavelet-like phenomena such as edge harmonic oscillations and quasi-coherent modes appear in a number of laboratory fusion plasmas [78–81]. Lastly, the systems of nonlinear ODEs identified by SINDy tend to have depreciating stability properties as the number of modes increases. Future machine learning work in nonlinear model identification techniques could focus on automated algorithms to search in the neighborhood of an identified SINDy model for a stable model with similar characteristics to the original model. Another route is to enforce additional physical or heuristic constraints requiring certain stability or limit cycle properties of the identified model, which may prove tractable for the specific case of models with only quadratic nonlinearities.

7 Acknowledgements

The authors would like to extend their gratitude to Dr. Uri Shumlak for manuscript comments. This work was supported by the Army Research Office (ARO W911NF-19-1-0045) and the Air Force Office of Scientific Research (AFOSR FA9550-18-1-0200). The simulations were supported by the U.S. Department of Energy, Office of Science, Office of Fusion Energy Sciences, under award number DE-SC0016256. This work was facilitated through the use of advanced computational, storage, and networking infrastructure provided by the Hyak supercomputer system.

Appendix A

Here we present linear and nonlinear models for the first $r = 7$ POD modes. The models are based on the same simulation data. The two SINDy models are fit on 80% of the simulation data from 1.5–4.0 ms, during which approximate power balance is satisfied in the simulation. The identified model is tested on the remaining 20% of the data.

A.1 Linear model

The pairwise POD mode trajectories in Fig. 2 indicate that mode pairs 1-2, 3-4, and 5-6 behave as nearly independent harmonic oscillators. A data-driven model restricted to linear terms correctly identifies a set of decoupled oscillators, but slightly misidentifies the true injector harmonics. This results in phase issues for long-time forecasting, as in Fig. 4. The seventh mode (not shown) is permitted to evolve with quadratic nonlinearities, but nonetheless drifts after a short time.

A.2 Nonlinear model

The more complex nonlinear model, presented in the main body of the paper, corrects the phase errors in the linear model. Nonlinear dynamics in the first six modes also benefit the forecast in the challenging seventh mode. However, this improvement is limited, since the first six models are strongly peaked at the harmonics of the injector, f_{inj} , and struggle to capture low-frequency content in the seventh mode. Nonlinearities are also required in order to capture deviations from a harmonic oscillator structure, such as those which can be seen visually for modes 5-6 in the pairwise feature space illustrations in Fig. 2.

The nonlinear model from Sec. 5 is shown in Fig. 5. Mode pair 1-2 forms a harmonic oscillator at $f_{\text{inj}} \approx 14.5$ kHz, and is decoupled from the rest of the system. This is expected because these modes primarily represent the forcing by the injectors. In fact, the model fits the dynamics of the third and fourth modes by forcing with modes 1-2. If we take as an initial condition $a_1(0) = F$ and $a_2(0) = 0$, then $a_1(t) = F \cos(\omega_{\text{inj}}t)$, $a_2(t) = -F \sin(\omega_{\text{inj}}t)$ and the system for modes 3-4 becomes

$$\begin{bmatrix} \dot{a}_3 \\ \dot{a}_4 \end{bmatrix} = -F^2 \begin{bmatrix} 1.490 \sin(2\omega_{\text{inj}}t) \\ 1.374 \cos(2\omega_{\text{inj}}t) \end{bmatrix} \rightarrow \begin{bmatrix} a_3 \\ a_4 \end{bmatrix} = \frac{F^2}{2\omega_{\text{inj}}} \begin{bmatrix} 1.490 \cos(2\omega_{\text{inj}}t) \\ -1.374 \sin(2\omega_{\text{inj}}t) \end{bmatrix}. \quad (31)$$

Thus, modes 3-4 are driven to produce the second injector harmonics. Substituting in the solutions for modes 1-4, the dynamics for modes 5-6 have a more complicated structure, given by

$$\begin{bmatrix} \dot{a}_5 \\ \dot{a}_6 \end{bmatrix} \approx 0.164 \begin{bmatrix} a_6 \\ -a_5 \end{bmatrix} + \frac{F^3}{2\omega_{\text{inj}}} \begin{bmatrix} -1.225 \cos(\omega_{\text{inj}}t) \sin(2\omega_{\text{inj}}t) - 1.270 \sin(\omega_{\text{inj}}t) \cos(2\omega_{\text{inj}}t) \\ -1.180 \cos(\omega_{\text{inj}}t) \cos(2\omega_{\text{inj}}t) + 1.140 \sin(\omega_{\text{inj}}t) \sin(2\omega_{\text{inj}}t) \end{bmatrix}. \quad (32)$$

Approximating the forcing terms in each component reduces the system to

$$\begin{bmatrix} \dot{a}_5 \\ \dot{a}_6 \end{bmatrix} \approx 0.164 \begin{bmatrix} a_6 \\ -a_5 \end{bmatrix} - \frac{F^3}{2\omega_{\text{inj}}} \begin{bmatrix} 1.248 \sin(3\omega_{\text{inj}}t) \\ 1.160 \cos(3\omega_{\text{inj}}t) \end{bmatrix}. \quad (33)$$

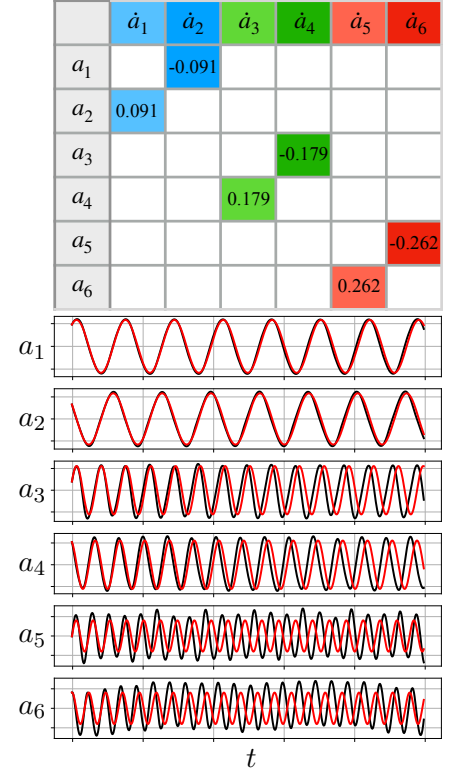


Figure 4: A linear model may slightly miss the f_{inj} harmonics, leading to errors in forecasting.

The solution is found straightforwardly with ansatz $a_5 = F_1 \cos(3\omega_{\text{inj}}t) + F_2 \sin(3\omega_{\text{inj}}t)$ for some constants F_1 and F_2 , so we can see this is externally forced to $3f_{\text{inj}}$. Mode seven is driven at a mix of $2f_{\text{inj}}$, $3f_{\text{inj}}$, $4f_{\text{inj}}$ and $5f_{\text{inj}}$. A solution can be found but is not particularly illuminating, especially because the low frequency component of this mode is very difficult to approximate with the other modes. Although we have added some model complexity, this nonlinear model avoids the phase errors seen with the simple linear model. Moreover, nonlinear models will be essential for plasma systems which have temporal modes that cannot be decomposed into sets of harmonic oscillators.

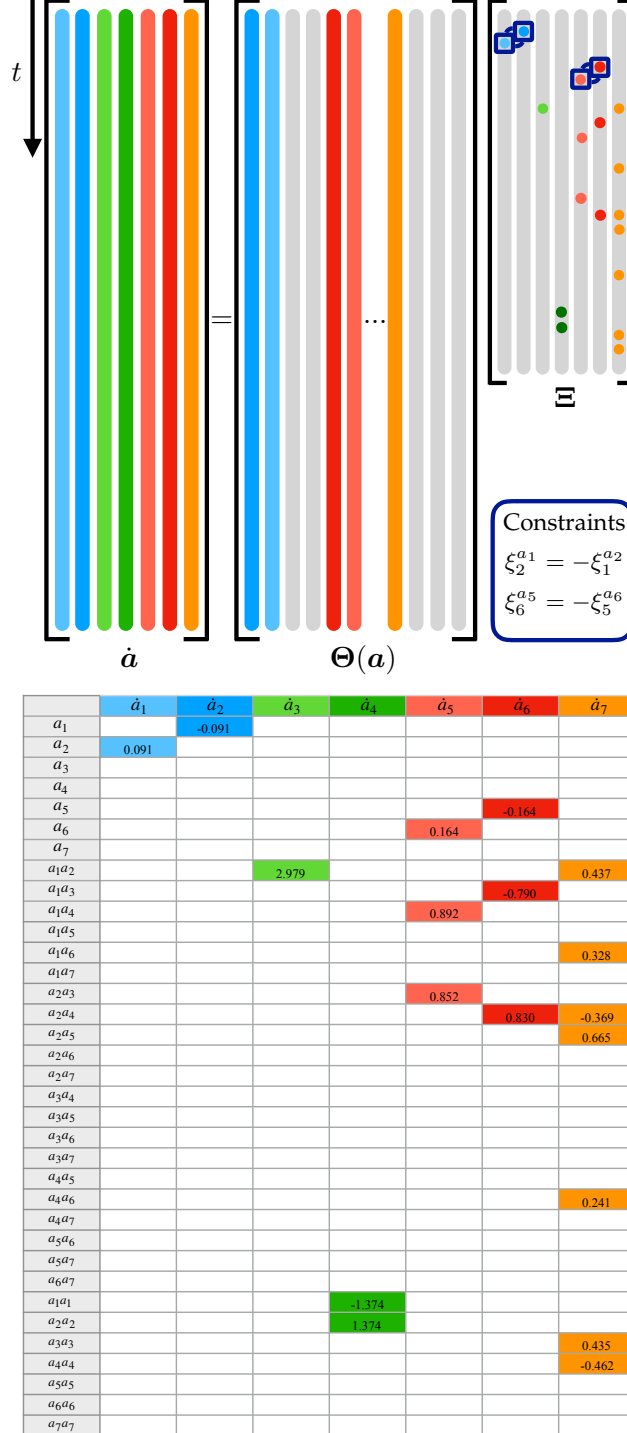


Figure 5: Constrained SINDy model describing the amplitudes of the first $r = 7$ POD modes.

References

- [1] J. R. Roth, *Industrial plasma engineering: Volume 2: Applications to nonthermal plasma processing*. CRC press, 2001, vol. 2.
- [2] D. E. Post, K. Borrass, and J. Callen, “ITER physics,” *International Atomic Energy Agency (IAEA)*, 1991.
- [3] A. Loarte, B. Lipschultz, A. Kukushkin, G. Matthews, P. Stangeby, N. Asakura, G. Counsell, G. Federici, A. Kallenbach, K. Krieger *et al.*, “Power and particle control,” *Nuclear Fusion*, vol. 47, no. 6, p. S203, 2007.
- [4] S. L. Brunton and J. N. Kutz, *Data-driven science and engineering: Machine learning, dynamical systems, and control*. Cambridge University Press, 2019.
- [5] F. Allgöwer, T. A. Badgwell, J. S. Qin, J. B. Rawlings, and S. J. Wright, “Nonlinear predictive control and moving horizon estimationan introductory overview,” in *Advances in control*. Springer, 1999, pp. 391–449.
- [6] E. Kaiser, J. N. Kutz, and S. L. Brunton, “Sparse identification of nonlinear dynamics for model predictive control in the low-data limit,” *Proceedings of the Royal Society A*, vol. 474, no. 2219, p. 20180335, 2018.
- [7] S. L. Brunton and B. R. Noack, “Closed-loop turbulence control: Progress and challenges,” *Applied Mechanics Reviews*, vol. 67, pp. 050 801–1–050 801–48, 2015.
- [8] P. J. Holmes, J. L. Lumley, G. Berkooz, and C. W. Rowley, *Turbulence, coherent structures, dynamical systems and symmetry*, 2nd ed., ser. Cambridge Monographs in Mechanics. Cambridge, England: Cambridge University Press, 2012.
- [9] K. Taira, S. L. Brunton, S. Dawson, C. W. Rowley, T. Colonius, B. J. McKeon, O. T. Schmidt, S. Gordeyev, V. Theofilis, and L. S. Ukeiley, “Modal analysis of fluid flows: An overview,” *AIAA Journal*, vol. 55, no. 12, pp. 4013–4041, 2017.
- [10] M. Pandya, “Low edge safety factor disruptions in the compact toroidal hybrid: Operation in the low-q regime, passive disruption avoidance and the nature of MHD precursors,” Ph.D. dissertation, Auburn University, 2016.
- [11] B. P. van Milligen, E. Sánchez, A. Alonso, M. A. Pedrosa, C. Hidalgo, A. M. de Aguilera, and A. L. Fraguas, “The use of the biorthogonal decomposition for the identification of zonal flows at TJ-II,” *Plasma Physics and Controlled Fusion*, vol. 57, no. 2, p. 025005, Dec. 2014.
- [12] P. J. Byrne, “Study of external kink modes in shaped hbt-ep plasmas,” Ph.D. dissertation, Columbia University, 2017.
- [13] A. A. Kaptanoglu, K. D. Morgan, C. J. Hansen, and S. L. Brunton, “Characterizing magnetized plasmas with dynamic mode decomposition,” *Physics of Plasmas*, vol. 27, no. 3, p. 032108, 2020.
- [14] S. L. Brunton, B. R. Noack, and P. Koumoutsakos, “Machine learning for fluid mechanics,” *To appear in Annual Review of Fluid Mechanics (arXiv preprint arXiv: 1905.11075)*, vol. 52, 2020.
- [15] B. R. Noack, K. Afanasiev, M. Morzynski, G. Tadmor, and F. Thiele, “A hierarchy of low-dimensional models for the transient and post-transient cylinder wake,” *Journal of Fluid Mechanics*, vol. 497, pp. 335–363, 2003.
- [16] P. Benner, S. Gugercin, and K. Willcox, “A survey of projection-based model reduction methods for parametric dynamical systems,” *SIAM review*, vol. 57, no. 4, pp. 483–531, 2015.
- [17] J. N. Kutz, S. L. Brunton, B. W. Brunton, and J. L. Proctor, *Dynamic Mode Decomposition: Data-Driven Modeling of Complex Systems*. SIAM, 2016.
- [18] B. R. Noack, W. Stankiewicz, M. Morzynski, and P. J. Schmid, “Recursive dynamic mode decomposition of a transient cylinder wake,” *Journal of Fluid Mechanics*, vol. 809, pp. 843–872, 2016.
- [19] K. Carlberg, M. Barone, and H. Antil, “Galerkin v. least-squares Petrov–Galerkin projection in nonlinear model reduction,” *Journal of Computational Physics*, vol. 330, pp. 693–734, 2017.
- [20] C. W. Rowley and S. T. Dawson, “Model reduction for flow analysis and control,” *Annual Review of Fluid Mechanics*, vol. 49, pp. 387–417, 2017.
- [21] T. Dudok de Wit, A.-L. Pecquet, J.-C. Vallet, and R. Lima, “The biorthogonal decomposition as a tool

- for investigating fluctuations in plasmas," *Physics of Plasmas*, vol. 1, no. 10, pp. 3288–3300, 1994.
- [22] J. Levesque, N. Rath, D. Shiraki, S. Angelini, J. Bialek, P. Byrne, B. DeBono, P. Hughes, M. Mauel, G. Navratil *et al.*, "Multimode observations and 3D magnetic control of the boundary of a tokamak plasma," *Nuclear Fusion*, vol. 53, no. 7, p. 073037, 2013.
 - [23] B. Victor, C. Akcay, C. Hansen, T. Jarboe, B. Nelson, and K. Morgan, "Development of validation metrics using biorthogonal decomposition for the comparison of magnetic field measurements," *Plasma Physics and Controlled Fusion*, vol. 57, no. 4, p. 045010, 2015.
 - [24] C. Hansen, B. Victor, K. Morgan, T. Jarboe, A. Hossack, G. Marklin, B. Nelson, and D. Sutherland, "Numerical studies and metric development for validation of magnetohydrodynamic models on the HIT-SI experiment," *Physics of Plasmas*, vol. 22, no. 5, p. 056105, 2015.
 - [25] P. J. Schmid, "Dynamic mode decomposition of numerical and experimental data," *Journal of Fluid Mechanics*, vol. 656, pp. 5–28, 2010.
 - [26] R. Taylor, J. N. Kutz, K. Morgan, and B. A. Nelson, "Dynamic mode decomposition for plasma diagnostics and validation," *Review of Scientific Instruments*, vol. 89, no. 5, p. 053501, 2018.
 - [27] C. W. Rowley, T. Colonius, and R. M. Murray, "Model reduction for compressible flows using POD and Galerkin projection," *Physica D: Nonlinear Phenomena*, vol. 189, no. 1-2, pp. 115–129, 2004.
 - [28] B. R. Noack, M. Schlegel, M. Morzynski, and G. Tadmor, *Galerkin method for nonlinear dynamics*. Springer, DMD 2011.
 - [29] M. J. Balajewicz, E. H. Dowell, and B. R. Noack, "Low-dimensional modelling of high-reynolds-number shear flows incorporating constraints from the navier–stokes equation," *Journal of Fluid Mechanics*, vol. 729, pp. 285–308, 2013.
 - [30] K. Carlberg, R. Tuminaro, and P. Boggs, "Preserving lagrangian structure in nonlinear model reduction with application to structural dynamics," *SIAM Journal on Scientific Computing*, vol. 37, no. 2, pp. B153–B184, 2015.
 - [31] M. Schlegel and B. R. Noack, "On long-term boundedness of galerkin models," *Journal of Fluid Mechanics*, vol. 765, pp. 325–352, 2015.
 - [32] S. L. Brunton, J. L. Proctor, and J. N. Kutz, "Discovering governing equations from data by sparse identification of nonlinear dynamical systems," *Proceedings of the National Academy of Sciences*, vol. 113, no. 15, pp. 3932–3937, 2016.
 - [33] J.-C. Loiseau and S. L. Brunton, "Constrained sparse Galerkin regression," *Journal of Fluid Mechanics*, vol. 838, pp. 42–67, 2018.
 - [34] J.-C. Loiseau, B. R. Noack, and S. L. Brunton, "Sparse reduced-order modeling: sensor-based dynamics to full-state estimation," *Journal of Fluid Mechanics*, vol. 844, pp. 459–490, 2018.
 - [35] R. Everson and L. Sirovich, "Karhunen–Loeve procedure for gappy data," *JOSA A*, vol. 12, no. 8, pp. 1657–1664, 1995.
 - [36] K. Willcox, "Unsteady flow sensing and estimation via the gappy proper orthogonal decomposition," *Computers & Fluids*, vol. 35, no. 2, pp. 208–226, 2006.
 - [37] S. Chaturantabut and D. C. Sorensen, "Discrete empirical interpolation for nonlinear model reduction," in *Proceedings of the 48th IEEE Conference on Decision and Control (CDC) held jointly with 2009 28th Chinese Control Conference*. IEEE, 2009, pp. 4316–4321.
 - [38] K. Carlberg, C. Farhat, J. Cortial, and D. Amsallem, "The GNAT method for nonlinear model reduction: effective implementation and application to computational fluid dynamics and turbulent flows," *Journal of Computational Physics*, vol. 242, pp. 623–647, 2013.
 - [39] Z. Drmac and S. Gugercin, "A new selection operator for the discrete empirical interpolation method—improved a priori error bound and extensions," *SIAM Journal on Scientific Computing*, vol. 38, no. 2, pp. A631–A648, 2016.
 - [40] B. M. de Silva, K. Champion, M. Quade, J.-C. Loiseau, J. N. Kutz, and S. L. Brunton, "Pysindy: A python package for the sparse identification of nonlinear dynamics from data," 2020.
 - [41] C. Galperti, C. Marchetto, E. Alessi, D. Minelli, M. Mosconi, F. Belli, L. Boncagni, A. Botrugno, P. Burratti, B. Esposito *et al.*, "Development of real-time MHD markers based on biorthogonal decomposition

- of signals from Mirnov coils," *Plasma Physics and Controlled Fusion*, vol. 56, no. 11, p. 114012, 2014.
- [42] A. Hossack, T. Jarboe, R. Chandra, K. Morgan, D. Sutherland, J. Penna, C. Everson, and B. Nelson, "Plasma response to sustainment with imposed-dynamo current drive in HIT-SI and HIT-SI3," *Nuclear Fusion*, vol. 57, no. 7, p. 076026, 2017.
 - [43] T. Jarboe, W. Hamp, G. Marklin, B. Nelson, R. O'Neill, A. Redd, P. Sieck, R. Smith, and J. Wrobel, "Spheromak formation by steady inductive helicity injection," *Physical review letters*, vol. 97, no. 11, p. 115003, 2006.
 - [44] J. Wesson and D. J. Campbell, *Tokamaks*. Oxford university press, 2011, vol. 149.
 - [45] L. Sirovich, "Turbulence and the dynamics of coherent structures. III. Dynamics and scaling," *Quarterly of Applied Mathematics*, vol. 45, no. 3, pp. 583–590, 1987.
 - [46] J. D. Huba, "Hall magnetohydrodynamics-a tutorial," in *Space Plasma Simulation*. Springer, 2003, pp. 166–192.
 - [47] L. Spitzer, *Physics of fully ionized gases*. Courier Corporation, 2006.
 - [48] B. R. Noack, K. Afanasiev, M. Morzyński, G. Tadmor, and F. Thiele, "A hierarchy of low-dimensional models for the transient and post-transient cylinder wake," *Journal of Fluid Mechanics*, vol. 497, pp. 335–363, 2003.
 - [49] M. Carini, F. Auteri, and F. Giannetti, "Centre-manifold reduction of bifurcating flows," *Journal of Fluid Mechanics*, vol. 767, pp. 109–145, 2015.
 - [50] S. Galtier, *Introduction to modern magnetohydrodynamics*. Cambridge University Press, 2016.
 - [51] M. Schmidt and H. Lipson, "Distilling free-form natural laws from experimental data," *Science*, vol. 324, no. 5923, pp. 81–85, 2009.
 - [52] R. Tibshirani, "Regression shrinkage and selection via the lasso," *Journal of the Royal Statistical Society. Series B (Methodological)*, pp. 267–288, 1996.
 - [53] P. Zheng, T. Askham, S. L. Brunton, J. N. Kutz, and A. Y. Aravkin, "A unified framework for sparse relaxed regularized regression: Sr3," *IEEE Access*, vol. 7, pp. 1404–1423, 2019.
 - [54] —, "A unified framework for sparse relaxed regularized regression: SR3," *IEEE Access*, vol. 7, pp. 1404–1423, 2018.
 - [55] J. S. Wrobel, *A study of HIT-SI plasma dynamics using surface magnetic field measurements*. University of Washington, 2011.
 - [56] C. Sovinec, A. Glasser, T. Gianakon, D. Barnes, R. Nebel, S. Kruger, D. Schnack, S. Plimpton, A. Tarditi, M.-S. Chu *et al.*, "Nonlinear magnetohydrodynamics simulation using high-order finite elements," *Journal of Computational Physics*, vol. 195, no. 1, pp. 355–386, 2004.
 - [57] V. Izzo and T. Jarboe, "A numerical assessment of the Lundquist number requirement for relaxation current drive," *Physics of Plasmas*, vol. 10, no. 7, pp. 2903–2911, 2003.
 - [58] C. Akcay, "Extended magnetohydrodynamic simulations of the helicity injected torus (HIT-SI) spheromak experiment with the NIMROD code," Ph.D. dissertation, University of Washington, Seattle, 2013.
 - [59] K. Morgan, T. Jarboe, A. Hossack, R. Chandra, and C. Everson, "Validation of extended magnetohydrodynamic simulations of the HIT-SI3 experiment using the NIMROD code," *Physics of Plasmas*, vol. 24, no. 12, p. 122510, 2017.
 - [60] K. Morgan, "Finite-beta simulations of HIT-SI and HIT-SI3 using the NIMROD code," Ph.D. dissertation, University of Washington, Seattle, 2018.
 - [61] K. Morgan, T. Jarboe, and C. Akcay, "Formation of closed flux surfaces in spheromaks sustained by steady inductive helicity injection," *Nuclear Fusion*, vol. 59, no. 6, p. 066037, 2019.
 - [62] J. N. Kutz, X. Fu, and S. L. Brunton, "Multiresolution dynamic mode decomposition," *SIAM Journal on Applied Dynamical Systems*, vol. 15, no. 2, pp. 713–735, 2016.
 - [63] M. Mendez, M. Balabane, and J.-M. Buchlin, "Multi-scale proper orthogonal decomposition of complex fluid flows," *Journal of Fluid Mechanics*, vol. 870, pp. 988–1036, 2019.
 - [64] D. Wroblewski, G. Jahns, and J. Leuer, "Tokamak disruption alarm based on a neural network model

- of the high-beta limit," *Nuclear Fusion*, vol. 37, no. 6, pp. 725–741, Jun 1997.
- [65] G. Pautasso, C. Tichmann, S. Egorov, T. Zehetbauer, O. Gruber, M. Maraschek, K.-F. Mast, V. Mertens, I. Perchermeier, G. Raupp, W. Treutterer, C. Windsor, and A. U. Team, "On-line prediction and mitigation of disruptions in ASDEX upgrade," *Nuclear Fusion*, vol. 42, no. 1, pp. 100–108, jan 2002.
 - [66] S. Dormido-Canto, J. Vega, J. Ramírez, A. Murari, R. Moreno, J. López, and A. P. and, "Development of an efficient real-time disruption predictor from scratch on JET and implications for ITER," *Nuclear Fusion*, vol. 53, no. 11, p. 113001, sep 2013.
 - [67] R. Aledda, B. Cannas, A. Fanni, A. Pau, and G. Sias, "Improvements in disruption prediction at ASDEX upgrade," *Fusion Engineering and Design*, vol. 96-97, pp. 698 – 702, 2015, proceedings of the 28th Symposium On Fusion Technology (SOFT-28).
 - [68] B. Cannas, P. C. de Vries, A. Fanni, A. Murari, A. Pau, and G. S. and, "Automatic disruption classification in JET with the ITER-like wall," *Plasma Physics and Controlled Fusion*, vol. 57, no. 12, p. 125003, oct 2015.
 - [69] A. Murari, M. Lungaroni, E. Peluso, P. Gaudio, J. Vega, S. Dormido-Canto, M. Baruzzo, and M. G. and, "Adaptive predictors based on probabilistic SVM for real time disruption mitigation on JET," *Nuclear Fusion*, vol. 58, no. 5, p. 056002, mar 2018. [Online]. Available: <https://doi.org/10.1088%2F1741-4326%2Faaaf9c>
 - [70] A. Pau, A. Fanni, B. Cannas, S. Carcangiu, G. Pisano, G. Sias, P. Sparapani, M. Baruzzo, A. Murari, F. Rimini, M. Tsalias, and P. C. de Vries, "A first analysis of JET plasma profile-based indicators for disruption prediction and avoidance," *IEEE Transactions on Plasma Science*, vol. 46, no. 7, pp. 2691–2698, July 2018.
 - [71] K. J. Montes, C. Rea, R. S. Granetz, R. A. Tinguely, N. Eidietis, O. M. Meneghini, D. L. Chen, B. Shen, B. J. Xiao, K. Erickson, and M. D. Boyer, "Machine learning for disruption warnings on Alcator C-Mod, DIII-D, and EAST," *Nuclear Fusion*, vol. 59, no. 9, p. 096015, July 2019.
 - [72] L. Lao, H. S. John, R. Stambaugh, A. Kellman, and W. Pfeiffer, "Reconstruction of current profile parameters and plasma shapes in tokamaks," *Nuclear fusion*, vol. 25, no. 11, p. 1611, 1985.
 - [73] S. M. Kaye, D. Battaglia, D. Baver, E. Belova, J. Berkery, V. N. Duarte, N. Ferraro, E. Fredrickson, N. Gorelenkov, W. Guttenfelder *et al.*, "NSTX/NSTX-U theory, modeling and analysis results," *Nuclear Fusion*, vol. 59, no. 11, p. 112007, 2019.
 - [74] C. Rea, R. S. Granetz, K. Montes, R. A. Tinguely, N. Eidietis, J. M. Hanson, and B. Sammulu, "Disruption prediction investigations using machine learning tools on DIII-D and Alcator C-Mod," *Plasma Physics and Controlled Fusion*, vol. 60, no. 8, p. 084004, June 2018.
 - [75] C. Rea and R. S. Granetz, "Exploratory machine learning studies for disruption prediction using large databases on DIII-D," *Fusion Science and Technology*, vol. 74, no. 1-2, pp. 89–100, 2018.
 - [76] K. Lee and K. T. Carlberg, "Model reduction of dynamical systems on nonlinear manifolds using deep convolutional autoencoders," *Journal of Computational Physics*, vol. 404, p. 108973, 2020.
 - [77] M. Farge and K. Schneider, "Wavelet transforms and their applications to MHD and plasma turbulence: a review," *Journal of Plasma Physics*, vol. 81, no. 6, 2015.
 - [78] T. Golfopoulos, B. LaBombard, R. Parker, W. Burke, E. Davis, R. Granetz, M. Greenwald, J. Irby, R. Leccacorvi, E. Marmor *et al.*, "External excitation of a short-wavelength fluctuation in the Alcator C-Mod edge plasma and its relationship to the quasi-coherent mode," *Physics of Plasmas*, vol. 21, no. 5, p. 056111, 2014.
 - [79] T. Golfopoulos, "The wavelet nature of persistent edge fluctuations observed on Alcator C-Mod," *Bulletin of the American Physical Society*, vol. 64, no. 11, 2019.
 - [80] K. Burrell, M. E. Austin, D. Brennan, J. DeBoo, E. Doyle, P. Gohil, C. Greenfield, R. Groebner, L. Lao, T. Luce *et al.*, "Quiescent H-mode plasmas in the DIII-D tokamak," *Plasma Physics and Controlled Fusion*, vol. 44, no. 5A, p. A253, 2002.
 - [81] E. Belonohy, G. Pokol, K. McCormick, G. Papp, and S. Zoletnik, "A systematic study of the quasi-coherent mode in the high density H-mode regime of Wendelstein 7-AS," *AIP Conference Proceedings*, vol. 993, no. 1, pp. 39–42, 2008.